

Four regimes of primary radiation damage in tungsten

J. Byggmästar,^{1,*} V-M. Yli-Suutala,^{2,1} A. Fellman,¹ J. Åström,^{3,1} J. Westerholm,² and F. Granberg¹

¹*Department of Physics, P.O. Box 43, FI-00014 University of Helsinki, Finland*

²*Faculty of Science and Engineering, Åbo Akademi University, Vattenborgsvägen 3, FI-20500 Åbo, Finland*

³*CSC – IT Center for Science Ltd., P.O. Box 405, 02101 Espoo, Finland*

(Dated: March 5, 2025)

We observe for the first time in silico the transition to a linear regime in the primary damage production in tungsten. As the critical plasma-facing material in fusion reactors, radiation damage in tungsten has been studied extensively in experiments and simulations. Irradiation experiments routinely produce recoils in the MeV range while full atomistic modelling has been limited to a few hundred keV. Here we bridge these scales with extremely large-scale and accurate machine-learning-driven molecular dynamics simulations with recoil energies up to 2 MeV in systems up to one billion atoms. We reveal four regimes of primary damage as a function of damage energy, with a transition to a high-energy regime that deviates from all previous models. Curiously, the start of the high-energy regime coincides with the highest possible recoil energy to tungsten atoms from fusion-emitted neutrons (300 keV).

Formation of primary radiation damage produced by energetic particles is the fundamental mechanism to understand when probing the irradiation resistance of a material [1]. The primary damage in tungsten is of particular importance as tungsten is the leading choice for the plasma-facing wall material of tokamak fusion reactors. Since the emergence of W as the main fusion reactor material, the radiation tolerance has been intensively studied experimentally and computationally [2–12]. The 14.1 MeV neutrons emitted from the fusion reactions will produce recoil energies up to 300 keV in the W lattice. Molecular dynamics (MD) simulations have been crucial in quantifying and in detail observing the defects of the primary damage. However, the chaotic nature of collision cascades requires large simulations. The largest full MD simulations have now reached 300 keV [13, 14], covering the entire fusion-relevant range, although what occurs at even higher energies remains unexplored.

Due to the lack of fusion-like neutron sources, irradiation experiments often use heavy-ion irradiation in the MeV range to emulate the damage produced in fusion reactors and to accumulate high doses quickly. Such heavy ions can produce recoil energies far higher than the 300 keV maximum from fusion-emitted neutrons. For example, Yi et al. [3] carried out extensive irradiation studies with 2 MeV self-ion irradiations, Wielunska et al. [6] used 20.3 MeV self-ions and 7.5 MeV Si ions (translating to W recoils up to 3.45 MeV), El-Atwani et al. used 3 MeV Cu ions [4] (up to 2.3 MeV W recoils), and Wang et al. used 6 MeV Cu ions (up to 4.6 MeV W recoils) [7]. Thus there is a wide gap between the experimentally and the so far computationally reached energy range. Crucially, it has been observed that collision cascades in heavy metals, like W, deviate upwards from the expected linear trend predicted by damage models at recoil energies above 50 keV [13, 15–17]. The mechanism behind this superlinear trend was suggested to be related to the proximity of subcascades [15]. When cascade splitting into sub-

TABLE I: Primary knock-on energies (E_{PKA}), the number of atoms in the simulated lattice (N_{atoms}), the length of the cubic simulation system (L), and the number of independent cascade simulations with randomly directed recoils (N_{sim}). The cascades are simulated as one recoil per simulation unless otherwise noted.

| E_{PKA} (keV) | N_{atoms} | L (nm) | N_{sim} |
|-----------------|---------------|----------|-------------------|
| 0.04–0.25 | 54 million | 95.6 | 1000 ^a |
| 0.3–1.0 | 16 million | 63.7 | 500 ^b |
| 2, 5 | 128,000 | 12.74 | 100 |
| 10, 20 | 1.024 million | 31.9 | 100 |
| 50 | 8.192 million | 51.0 | 100 |
| 100 | 16 million | 63.7 | 100 |
| 200 | 54 million | 95.6 | 50 |
| 300, 500 | 128 million | 127 | 50 |
| 1000, 2000 | 1.024 billion | 255 | 20 |

^a 1000 recoils in one simulation. ^b 125 recoils in four independent simulations.

cascades occurs in heavy metals, the subcascades are often so close that the shock waves they produce in the W lattice overlap and result in large defect clusters and hence in more defects than expected [15]. The same authors also speculate that at even higher energies, the subcascades should become fully separated and the damage production should return to a linear trend. This transition has so far not been observed and the final high-energy linear trend not quantified. The critical question is at which energy this transition occurs relative to the fusion-neutron recoil spectrum (up to 300 keV) and typical heavy-ion irradiation experiments (>MeV), since it dictates how analogous heavy-ion radiation damage is to neutron-induced damage.

We here resolve this issue using extremely large-scale and accurate molecular dynamics simulations with a

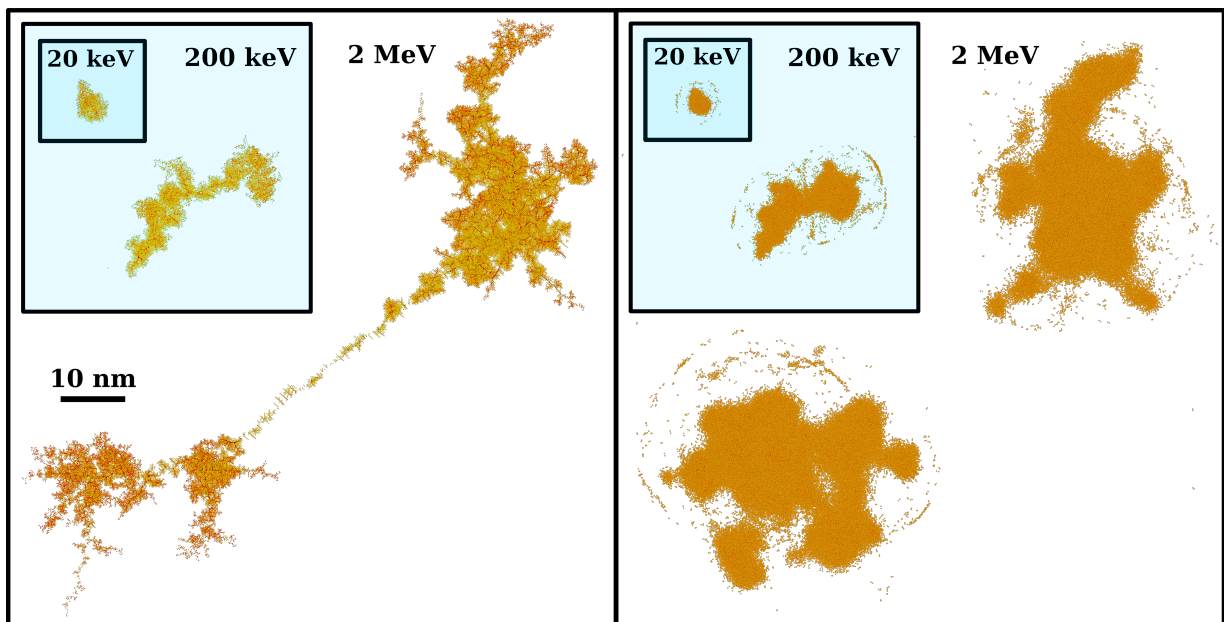


FIG. 1: Typical collision cascades across three orders of magnitude in recoil energies. Atoms with kinetic energies above 1 eV are shown and atoms are colored according to their kinetic energy (red: high, yellow: low). On the left, the cascades are visualised as all high-energy atoms up to times just before the heat spike (150, 170, and 190 fs for 20 keV, 200 keV, and 2 MeV, respectively) to show typical structures and sizes. On the right, the same cascades are shown as all high-energy atoms at a time during the heat spike and the emission of shock waves (1.0, 1.7, 3.3 ps, respectively), revealing three different types of cascades; single cascade, overlapping subcascades, and fully separated subcascades.

machine-learned interatomic potential to reach unprecedented damage energies with full atomistic resolution. We achieve this by implementing the computationally efficient tabulated Gaussian approximation potential (tab-GAP) [18] to run on GPU hardware through the Kokkos library [19] and LAMMPS [20]. We then perform molecular dynamics simulations with primary knock-on atom (PKA) energies across six orders of magnitude, from 40 eV to 2 MeV, to obtain the primary damage production trend for all practically relevant energies. Containing the collision cascades within the simulation cell required W lattices up to one billion atoms for the highest PKA energies (1 and 2 MeV). The systems are initially relaxed to 300 K and zero pressure. In the cascade simulations, we use an adaptive time step, a total simulation time of 50 ps, and the *NVE* ensemble for all atoms except for those in a 8 Å thick border region for which the Nosé-Hoover thermostat (300 K) is applied. The border thermostat dissipates heat and dampens shock waves from the cascade to avoid unphysical cascade self-interaction. For high energies, the energy loss to electronic excitations becomes significant. We consider electronic stopping as a friction force for atoms with kinetic energies above 10 eV using data from SRIM [21]. The PKA energies, system sizes, and number of cascade simulations are summarised in Tab. I. The directions of the independent recoils are sampled randomly. The simulations are carried out on

the GPU nodes of the LUMI supercomputer. The damage is analysed using Wigner-Seitz analysis for finding vacancies and self-interstitial atoms (SIAs), dislocation extraction algorithm (DXA) for finding dislocations, and cluster analysis to get cluster size statistics, all implemented in and visualised using OVITO [22, 23].

Fig. 1 shows typical collision cascades spanning three orders of magnitude in recoil energy. By analysing the cascade evolution, morphology, and the final surviving primary damage, we group the damage production into four regimes as a function of energy. The four energy regimes are visualised in the number of Frenkel pairs in Fig. 2. The first two regimes follow the arc-dpa model [16] with the low-energy correction [24] and are well understood. The first regime spans near-threshold displacement energies (TDE). The lowest TDE in W is around 40 eV for recoils close to the $\langle 100 \rangle$ or $\langle 111 \rangle$ directions, which is known from experiments and reproduced well by the machine-learned potential used here [25]. The average TDE over all crystal directions is 95 eV and the maximum exceeds 250 eV [25]. For energies around the average TDE, at 80–130 eV, there is a plateau where approximately 0.25 Frenkel pairs are produced on average per recoil, similar to what has been observed experimentally in Cu [26]. The production of on average at least one Frenkel pair occurs for energies above 500 eV, highlighting the efficient defect recombination for energies far

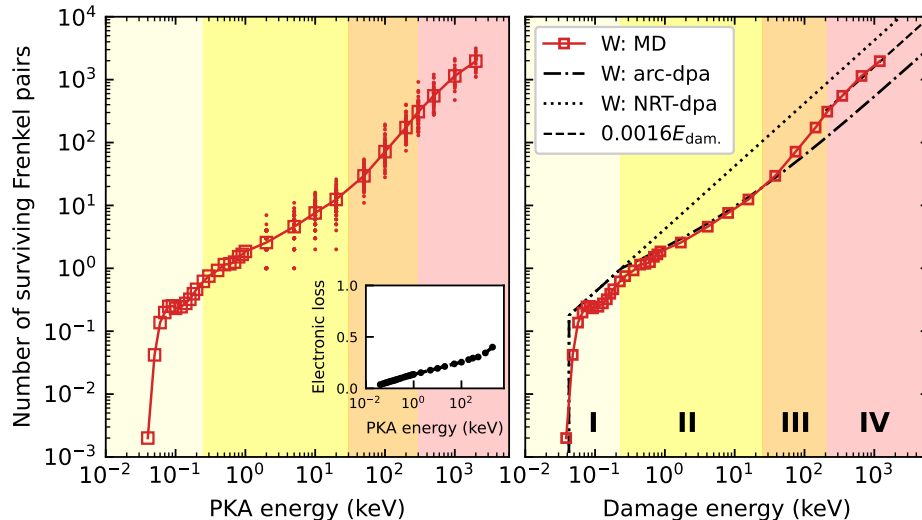


FIG. 2: Number of Frenkel pairs formed as a function of PKA energy (left) and damage energy (right). The damage energy is the PKA energy minus the energy loss to electronic stopping, the fractions of which is shown in the inset figure. The highest PKA energy 2 MeV corresponds to, on average, 1.2 MeV damage energy. The damage production is grouped into four regimes, I: near-threshold energies with on average less than one defect produced, II: single cascades following the arc-dpa model, III: transition region with superlinear damage trend caused by overlapping subcascades, and IV: the final linear regime observed for the first time in W here, where subcascades are fully separated and the damage production becomes linear. The NRT-dpa and arc-dpa models [16] with the low-energy correction [24] are plotted for comparison as well as the final regime-IV linear trend.

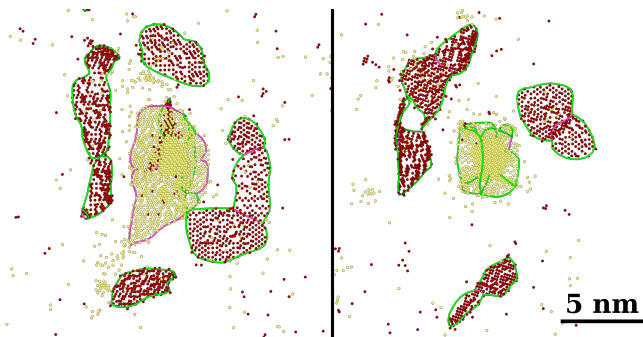


FIG. 3: Two examples of large vacancy clusters surrounded by interstitial-type dislocation loops produced by 2 MeV cascades. Vacancies are colored yellow, self-interstitial atoms red, $1/2\langle 111 \rangle$ dislocation lines green and $\langle 100 \rangle$ dislocations pink.

above TDEs.

The second sublinear regime is characterised by conventional collision cascades with increasingly strong heat spikes but no clear subcascade splitting, exemplified by the 20 keV cascade in Fig. 1. Our data for this regime agrees well with the arc-dpa equation fitted to MD data in Ref. [16] after increasing the average TDE to 95 eV.

The third superlinear regime agrees with the observations in Ref. [15] and starts at around 20–30 keV. At these energies and above, subcascade splitting become

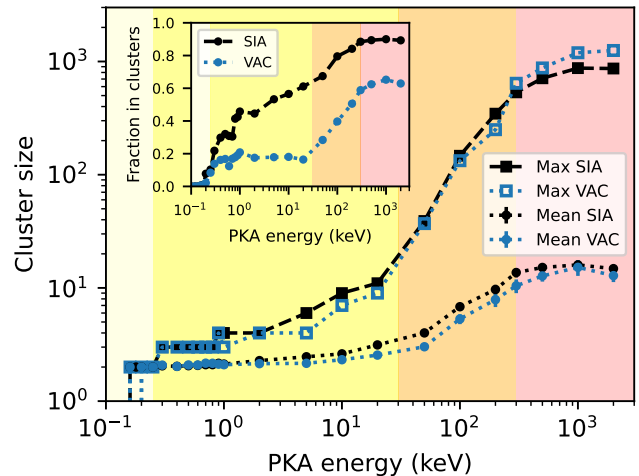


FIG. 4: Defect cluster statistics as functions of PKA energy: maximum and mean cluster sizes of vacancy and self-interstitial clusters, and the fraction of vacancies and self-interstitials in clusters (inset figure). The figures are by background color grouped into the same four regimes discussed in the text.

increasingly likely, but the subcascades remain close in proximity and partially overlap. The overlap causes the heat spikes and shock waves to interact, which often leads

to large defect clusters in forms of voids and vacancy dislocation loops surrounded by self-interstitial loops. The overlapping shockwaves are visible in the 200 keV cascade in Fig. 1. Examples of large defect cluster groups are shown in Fig. 3. The largest vacancy clusters often consist of a void-like core with dislocation lines attached or individual large dislocation loops. Vacancy dislocation loops with both $\langle 100 \rangle$ and $1/2\langle 111 \rangle$ Burgers vectors are frequently formed. Self-interstitial clusters are almost exclusively dislocation loops with the $1/2\langle 111 \rangle$ Burgers vector, in line with previous studies [8, 12]. The statistics of the cascade-produced dislocations are shown in the Supplemental material.

The fourth linear regime is for the first time revealed and quantified here. For energies above 300 keV, most cascades split into large subcascades that are far enough apart not to interact significantly. The subcascades themselves may still produce partially overlapping regime-III (sub)subcascades, but the increasingly separated and noninteracting large subcascades result in the expected linear trend.

The four regimes become more clear when analysing the statistics of defect clusters produced by cascades at different energies, summarised in Fig. 4. The formation of larger and larger vacancy and self-interstitial clusters in the superlinear regime III is clear from Fig. 4. When reaching regime IV, the distribution of cluster sizes, including the mean and the maximum sizes, plateaus since the cascades split into smaller fully separated subcascades equivalent to lower-energy cascades. The fraction of vacancies and interstitials in clusters, shown in the inset figure of Fig. 4, shows a similar overall trend, with a plateau or slowly increasing clustered fraction at low energies, a rapid increase in regime III and plateauing to a constant in regime IV.

Fig. 4 suggests that the largest clusters that frequently can form directly from collision cascades in pristine bulk tungsten is around 1000 vacancies or self-interstitials. Clusters of that size are 4–10 nm in width depending on morphology. Previous simulations and experiments have confirmed that the frequency of forming clusters of given sizes follow power laws for small cluster sizes [8, 27]. Sand et al. later developed and experimentally validated a correction to the power law for large clusters that at the time were not reachable by simulations [9]. That model predicts an upper limit for the cluster size, which our simulations now directly confirm. The upper limit is also supported by experiments by Ciupiński et al., who used 20 MeV self-ion irradiation and observed dislocation loops only around 5 nm in size at low dose [28], translating to similar maximum cluster sizes that we observe here. Cluster distributions from the simulations for all energies are provided in the Supplemental material. We also note that while the mean size of the clusters is always higher for interstitials, the largest vacancy clusters become larger than the largest interstitial clusters at the

highest damage energies. The opposite is true for low energies, and regime III is the transition region also in this case. The clustered fractions in the inset of Fig. 4 reflect the same trend. At low energies, around half of interstitials formed directly by the cascades are in clusters while only 15–20% of vacancies are clustered. The transition regime III marks a sharp increase in both, and at high energies almost all interstitials and around 60% of vacancies are in clusters, most of them in large clusters similar to those in Fig. 3.

To conclude, we have here provided accurate data for the primary radiation damage of tungsten across all relevant energies, from the threshold displacement energy 40 eV up to 2 MeV, with a simple linear trend that extrapolates to even higher energies. Strikingly, the final linear regime IV revealed and characterised here starts at around 300 keV, coinciding with the highest recoil energy from 14.1 MeV fusion neutrons. This can be considered a fortunate coincidence, because it means that even in high-energy heavy-ion irradiation experiments with recoils beyond fusion relevancy, the induced collision cascades split and behave similarly to fusion-relevant recoils and the extent of the primary damage can be linearly extrapolated from the high-energy data of Figs. 2 and 4.

Acknowledgments. JB and FG acknowledge funding from the Research council of Finland through the OCRAMLIP (grant number 354234) and the DEVHIS (grant number 340538) projects, respectively. This work has been partially carried out under the EUROfusion E-TASC Advanced Computing Hub project. This work has partially been carried out within the framework of the EUROfusion Consortium, funded by the European Union via the Euratom Research and Training Programme (Grant Agreement No 101052200 — EUROfusion). Views and opinions expressed are however those of the author(s) only and do not necessarily reflect those of the European Union or the European Commission. Neither the European Union nor the European Commission can be held responsible for them. We acknowledge University of Helsinki, Finland for awarding this project access to the LUMI supercomputer, owned by the EuroHPC Joint Undertaking, hosted by CSC (Finland) and the LUMI consortium.

* Corresponding author; jesper.byggmatar@helsinki.fi

- [1] K. Nordlund, S. J. Zinkle, A. E. Sand, F. Granberg, R. S. Averback, R. E. Stoller, T. Suzudo, L. Malerba, F. Banhart, W. J. Weber, F. Willaime, S. L. Dudarev, and D. Simeone, Primary radiation damage: A review of current understanding and models, *Journal of Nuclear Materials* **512**, 450 (2018).
- [2] X. Yi, M. L. Jenkins, M. A. Kirk, Z. Zhou, and S. G. Roberts, In-situ TEM studies of 150 keV W⁺ ion irradiated W and W-alloys: Damage production and mi-

- crostructural evolution, *Acta Materialia* **112**, 105 (2016).
- [3] X. Yi, M. L. Jenkins, K. Hattar, P. D. Edmondson, and S. G. Roberts, Characterisation of radiation damage in W and W-based alloys from 2MeV self-ion near-bulk implantations, *Acta Materialia* **92**, 163 (2015).
- [4] O. El-Atwani, E. Esquivel, M. Efe, E. Aydogan, Y. Q. Wang, E. Martinez, and S. A. Maloy, Loop and void damage during heavy ion irradiation on nanocrystalline and coarse grained tungsten: Microstructure, effect of dpa rate, temperature, and grain size, *Acta Materialia* **149**, 206 (2018).
- [5] Z. Zhang, K. Yabuuchi, and A. Kimura, Defect distribution in ion-irradiated pure tungsten at different temperatures, *Journal of Nuclear Materials* **480**, 207 (2016).
- [6] B. Wielunska, T. Płociński, T. Schwarz-Selinger, M. Mayer, W. Jacob, and L. Ciupiński, Dislocation structure of tungsten irradiated by medium to high-mass ions, *Nuclear Fusion* **62**, 096003 (2022).
- [7] S. Wang, W. Guo, T. Schwarz-Selinger, Y. Yuan, L. Ge, L. Cheng, X. Zhang, X. Cao, E. Fu, and G.-H. Lu, Dynamic equilibrium of displacement damage defects in heavy-ion irradiated tungsten, *Acta Materialia* **244**, 118578 (2023).
- [8] A. E. Sand, S. L. Dudarev, and K. Nordlund, High-energy collision cascades in tungsten: Dislocation loops structure and clustering scaling laws, *EPL* **103**, 46003 (2013).
- [9] A. E. Sand, D. R. Mason, A. D. Backer, X. Yi, S. L. Dudarev, and K. Nordlund, Cascade fragmentation: Deviation from power law in primary radiation damage, *Materials Research Letters* **5**, 357 (2017).
- [10] D. R. Mason, A. E. Sand, X. Yi, and S. L. Dudarev, Direct observation of the spatial distribution of primary cascade damage in tungsten, *Acta Materialia* **144**, 905 (2018).
- [11] W. Setyawan, G. Nandipati, K. J. Roche, H. L. Heinisch, B. D. Wirth, and R. J. Kurtz, Displacement cascades and defects annealing in tungsten, Part I: Defect database from molecular dynamics simulations, *Journal of Nuclear Materials* **462**, 329 (2015).
- [12] F. Granberg, J. Byggmästar, and K. Nordlund, Molecular dynamics simulations of high-dose damage production and defect evolution in tungsten, *Journal of Nuclear Materials* **556**, 153158 (2021).
- [13] J. Fu, Y. Chen, J. Fang, N. Gao, W. Hu, C. Jiang, H.-B. Zhou, G.-H. Lu, F. Gao, and H. Deng, Molecular dynamics simulations of high-energy radiation damage in W and W-Re alloys, *Journal of Nuclear Materials* **524**, 9 (2019).
- [14] L. Liu, R. Qiu, Y. Chen, M. Jiang, N. Gao, B. Huang, F. Gao, W. Hu, and H. Deng, Displacement cascades database from molecular dynamics simulations in tungsten, *Journal of Nuclear Materials* **580**, 154415 (2023).
- [15] W. Setyawan, A. P. Selby, N. Juslin, R. E. Stoller, B. D. Wirth, and R. J. Kurtz, Cascade morphology transition in bcc metals, *Journal of Physics: Condensed Matter* **27**, 225402 (2015).
- [16] K. Nordlund, S. J. Zinkle, A. E. Sand, F. Granberg, R. S. Averback, R. Stoller, T. Suzudo, L. Malerba, F. Banhart, W. J. Weber, F. Willaime, S. L. Dudarev, and D. Simeone, Improving atomic displacement and replacement calculations with physically realistic damage models, *Nature Communications* **9**, 1084 (2018).
- [17] J. Liu, J. Byggmästar, Z. Fan, P. Qian, and Y. Su, Large-scale machine-learning molecular dynamics simulation of primary radiation damage in tungsten, *Physical Review B* **108**, 054312 (2023).
- [18] J. Byggmästar, K. Nordlund, and F. Djurabekova, Simple machine-learned interatomic potentials for complex alloys, *Physical Review Materials* **6**, 083801 (2022).
- [19] C. R. Trott, D. Lebrun-Grandié, D. Arndt, J. Ciesko, V. Dang, N. Ellingwood, R. Gayatri, E. Harvey, D. S. Hollman, D. Ibanez, N. Liber, J. Madsen, J. Miles, D. Poliakoff, A. Powell, S. Rajamanickam, M. Simberg, D. Sunderland, B. Turcksin, and J. Wilke, Kokkos 3: Programming model extensions for the exascale era, *IEEE Transactions on Parallel and Distributed Systems* **33**, 805 (2022).
- [20] A. P. Thompson, H. M. Aktulga, R. Berger, D. S. Bolintineanu, W. M. Brown, P. S. Crozier, P. J. in 't Veld, A. Kohlmeyer, S. G. Moore, T. D. Nguyen, R. Shan, M. J. Stevens, J. Tranchida, C. Trott, and S. J. Plimpton, LAMMPS - a flexible simulation tool for particle-based materials modeling at the atomic, meso, and continuum scales, *Computer Physics Communications* **271**, 108171 (2022).
- [21] J. F. Ziegler, M. D. Ziegler, and J. P. Biersack, SRIM - The stopping and range of ions in matter (2010), *Nuclear Instruments and Methods in Physics Research Section B: Beam Interactions with Materials and Atoms 19th International Conference on Ion Beam Analysis*, **268**, 1818 (2010).
- [22] A. Stukowski, Visualization and analysis of atomistic simulation data with OVITO—the Open Visualization Tool, *Modelling and Simulation in Materials Science and Engineering* **18**, 015012 (2010).
- [23] A. Stukowski, V. V. Bulatov, and A. Arsenlis, Automated identification and indexing of dislocations in crystal interfaces, *Modelling and Simulation in Materials Science and Engineering* **20**, 085007 (2012).
- [24] Q. Yang and P. Olsson, Full energy range primary radiation damage model, *Physical Review Materials* **5**, 073602 (2021).
- [25] J. Byggmästar, F. Djurabekova, and K. Nordlund, Threshold displacement energies in refractory high-entropy alloys, *Physical Review Materials* **8**, 115406 (2024).
- [26] W. E. King, K. L. Merkle, and M. Meshii, Threshold energy surface and frenkel pair resistivity for Cu, *Journal of Nuclear Materials* **117**, 12 (1983).
- [27] X. Yi, A. E. Sand, D. R. Mason, M. A. Kirk, S. G. Roberts, K. Nordlund, and S. L. Dudarev, Direct observation of size scaling and elastic interaction between nano-scale defects in collision cascades, *EPL* **110**, 36001 (2015).
- [28] L. Ciupiński, O. V. Ogorodnikova, T. Płociński, M. Andrzejczuk, M. Rasiński, M. Mayer, and K. J. Kurzydłowski, TEM observations of radiation damage in tungsten irradiated by 20 MeV W ions, *Nuclear Instruments and Methods in Physics Research Section B: Beam Interactions with Materials and Atoms Proceedings of the 19th International Workshop on Inelastic Ion-Surface Collisions (IISC-19)*, Frauenchiemsee, Germany, 16-21 September 2012, **317**, 159 (2013).

Supplemental information of: Four regimes of primary radiation damage in tungsten

J. Byggmästar,^{1,*} V-M. Yli-Suutala,^{2,1} A. Fellman,¹ J. Åström,^{3,1} J. Westerholm,² and F. Granberg¹

¹*Department of Physics, P.O. Box 43, FI-00014 University of Helsinki, Finland*

²*Faculty of Science and Engineering, Åbo Akademi University, Vattenborgsvägen 3, FI-20500 Åbo, Finland*

³*CSC – IT Center for Science Ltd., P.O. Box 405, 02101 Espoo, Finland*

(Dated: March 5, 2025)

GPU IMPLEMENTATION OF tabGAP

We ported the LAMMPS component of tabGAP (<https://gitlab.com/jezper/tabgap>) to GPUs using the Kokkos library [?]. The force computation is parallelized over the atoms. For simulations of one element, the Kokkos version of the code is 1.6 times faster when run on one GCD of an AMD MI250x GPU, compared to the original non-GPU code run on a full CPU node on LUMI with 128 AMD EPYC 7763 cores.

The force computation is performed on three atoms at once using a three-dimensional spline interpolation. The elements of the three atoms, along with their relative positions, determine which spline coefficients are to be used to compute the force on them. When more chemical elements are added to a simulation utilizing tabGAP as the interatomic potential, the performance degrades. This is because reading more different spline coefficients from memory leads to worse cache utilization. To help improve the performance of simulations with multiple elements, the neighbor list of each atom is sorted by element. A list of atoms sorted by element is also constructed. The force computation then loops over the sorted atoms and neighbors. Sorting the neighbors and atoms improves performance by 1.4x for simulations of five elements, each with an equal number of atoms distributed uniformly in the simulation box. The code is available open source (<https://gitlab.com/jezper/tabgap>) and easily compiled with LAMMPS.

We also ported the friction force electronic stopping routine of LAMMPS to Kokkos (`fix electron/stopping`) to allow all frequent computations needed in cascade simulations to be run on GPU.

SUPPLEMENTAL ANIMATIONS

The supplemental material contains animations of the representative cascade simulations showed in Fig. 1 in the main text. In the files with `ekin` in the file names, atoms with high kinetic energies are shown, to visualise the cascade structure and shock waves. In the files with `ws` in the file names, vacancies (blue) and interstitial atoms (yellow) identified by Wigner-Seitz analysis are shown, to visualise the formation of the final defect clusters. Note that due to the adaptive time step used in the simulations, the simulation time interval between animated frames is not constant (short time span in the beginning due to strong collisions and faster time evolution during the heat spike and until the end).

CASCADE RESULTS

Below, the key data from the cascade simulations are given in copyable plain text. The columns are: PKA energy in keV E_{PKA} , damage energy E_{dam} , average number of Frenkel pairs N_{FP} , standard deviation of N_{FP} , standard error of N_{FP} , maximum interstitial cluster size max_sia^a , mean interstitial cluster size $mean_sia$, maximum vacancy cluster size max_vac , mean vacancy cluster size $mean_vac$, fraction of interstitials in clusters cf_sia , fraction of vacancies in clusters cf_vac , number of simulated recoils N_{sim} , number of atoms per recoil in the system N_{atoms}^b , and average computational cost (GPU-hours) per cascade $GPUh$. The GPUs were AMD MI250x GPUs on the LUMI supercomputer in all simulations.

^aA cluster is defined as containing two or more vacancies or interstitials (so that a maximum size 0 means that all defects are isolated).

^bNumber of atoms per recoil. For energies 40–250 eV, 1000 recoils were placed on a grid and simulated simultaneously in a box of 54 million atoms. For 300–1000 eV, 125 recoils were simulated simultaneously in a box of 16 million atoms. For all higher energies, each recoil is simulated in a separate system of the given size.

| E_{PKA} (keV) | E_{dam} (keV) | N_{FP} | stddev | stderr | max_sia | $mean_sia$ | max_vac | $mean_vac$ | cf_sia | cf_vac | N_{sim} | N_{atoms} | $GPUh$ |
|-----------------|-----------------|----------|--------|--------|------------|-------------|------------|-------------|-----------|-----------|-----------|-------------|--------|
| 0.04 | 0.04 | 0.002 | 0.00 | 0.00 | 0 | 0.000 | 0 | 0.000 | 0.000 | 0.000 | 1000 | 5.400e+04 | 0.007 |
| 0.05 | 0.05 | 0.042 | 0.00 | 0.00 | 0 | 0.000 | 0 | 0.000 | 0.000 | 0.000 | 1000 | 5.400e+04 | 0.007 |
| 0.06 | 0.06 | 0.137 | 0.00 | 0.00 | 0 | 0.000 | 0 | 0.000 | 0.000 | 0.000 | 1000 | 5.400e+04 | 0.007 |
| 0.07 | 0.07 | 0.198 | 0.00 | 0.00 | 0 | 0.000 | 0 | 0.000 | 0.000 | 0.000 | 1000 | 5.400e+04 | 0.007 |
| 0.08 | 0.08 | 0.248 | 0.00 | 0.00 | 0 | 0.000 | 0 | 0.000 | 0.000 | 0.000 | 1000 | 5.400e+04 | 0.007 |
| 0.09 | 0.08 | 0.253 | 0.00 | 0.00 | 0 | 0.000 | 0 | 0.000 | 0.000 | 0.000 | 1000 | 5.400e+04 | 0.007 |
| 0.10 | 0.09 | 0.231 | 0.00 | 0.00 | 0 | 0.000 | 0 | 0.000 | 0.000 | 0.000 | 1000 | 5.400e+04 | 0.007 |
| 0.12 | 0.11 | 0.245 | 0.00 | 0.00 | 0 | 0.000 | 0 | 0.000 | 0.000 | 0.000 | 1000 | 5.400e+04 | 0.007 |
| 0.14 | 0.13 | 0.277 | 0.00 | 0.00 | 0 | 0.000 | 0 | 0.000 | 0.000 | 0.000 | 1000 | 5.400e+04 | 0.007 |
| 0.16 | 0.15 | 0.322 | 0.00 | 0.00 | 2 | 2.000 | 2 | 2.000 | 0.006 | 0.006 | 1000 | 5.400e+04 | 0.007 |
| 0.18 | 0.17 | 0.394 | 0.00 | 0.00 | 2 | 2.000 | 0 | 0.000 | 0.010 | 0.000 | 1000 | 5.400e+04 | 0.007 |
| 0.20 | 0.18 | 0.464 | 0.00 | 0.00 | 2 | 2.000 | 2 | 2.000 | 0.078 | 0.022 | 1000 | 5.400e+04 | 0.007 |
| 0.25 | 0.23 | 0.62 | 0.00 | 0.00 | 2 | 2.000 | 2 | 2.000 | 0.103 | 0.084 | 1000 | 5.400e+04 | 0.007 |
| 0.30 | 0.27 | 0.752 | 0.00 | 0.00 | 3 | 2.050 | 3 | 2.080 | 0.218 | 0.138 | 500 | 1.280e+05 | 0.017 |
| 0.40 | 0.36 | 0.926 | 0.00 | 0.00 | 3 | 2.029 | 3 | 2.027 | 0.298 | 0.162 | 500 | 1.280e+05 | 0.017 |
| 0.50 | 0.44 | 1.144 | 0.00 | 0.00 | 3 | 2.056 | 3 | 2.087 | 0.320 | 0.168 | 500 | 1.280e+05 | 0.017 |
| 0.60 | 0.53 | 1.18 | 0.00 | 0.00 | 3 | 2.068 | 3 | 2.086 | 0.308 | 0.124 | 500 | 1.280e+05 | 0.017 |
| 0.70 | 0.61 | 1.254 | 0.00 | 0.00 | 3 | 2.099 | 3 | 2.163 | 0.305 | 0.169 | 500 | 1.280e+05 | 0.017 |
| 0.80 | 0.70 | 1.524 | 0.00 | 0.00 | 3 | 2.100 | 3 | 2.159 | 0.414 | 0.178 | 500 | 1.280e+05 | 0.017 |
| 0.90 | 0.78 | 1.666 | 0.00 | 0.00 | 4 | 2.159 | 4 | 2.120 | 0.425 | 0.191 | 500 | 1.280e+05 | 0.017 |
| 1.00 | 0.86 | 1.854 | 0.00 | 0.00 | 4 | 2.126 | 3 | 2.098 | 0.458 | 0.208 | 500 | 1.280e+05 | 0.017 |
| 2.00 | 1.69 | 2.57 | 1.17 | 0.12 | 4 | 2.280 | 4 | 2.143 | 0.445 | 0.175 | 100 | 1.280e+05 | 0.020 |
| 5.00 | 4.12 | 4.59 | 1.97 | 0.20 | 6 | 2.465 | 4 | 2.158 | 0.533 | 0.179 | 100 | 1.280e+05 | 0.021 |
| 10.00 | 8.06 | 7.59 | 2.93 | 0.29 | 9 | 2.616 | 7 | 2.322 | 0.565 | 0.181 | 100 | 1.024e+06 | 0.142 |
| 20.00 | 15.74 | 12.43 | 4.38 | 0.44 | 11 | 3.136 | 9 | 2.550 | 0.611 | 0.164 | 100 | 1.024e+06 | 0.146 |
| 50.00 | 38.10 | 29.5 | 8.00 | 0.80 | 39 | 4.004 | 37 | 3.022 | 0.674 | 0.284 | 100 | 8.192e+06 | 1.250 |
| 100.00 | 74.54 | 71.54 | 28.20 | 2.82 | 147 | 6.824 | 133 | 5.318 | 0.795 | 0.397 | 100 | 1.600e+07 | 2.750 |
| 200.00 | 144.18 | 173.04 | 75.45 | 10.67 | 346 | 9.684 | 250 | 7.879 | 0.841 | 0.505 | 50 | 5.400e+07 | 10.667 |
| 300.00 | 211.94 | 309.7 | 154.72 | 21.88 | 534 | 13.671 | 642 | 10.438 | 0.884 | 0.588 | 50 | 1.280e+08 | 32.000 |
| 500.00 | 347.41 | 552.76 | 216.74 | 30.65 | 711 | 15.157 | 877 | 12.754 | 0.894 | 0.624 | 50 | 1.280e+08 | 40.000 |
| 1000.00 | 655.98 | 1145.2 | 433.27 | 96.88 | 874 | 15.978 | 1195 | 15.200 | 0.900 | 0.652 | 20 | 1.024e+09 | 725.00 |
| 2000.00 | 1198.25 | 1967.45 | 588.34 | 131.56 | 867 | 14.799 | 1251 | 12.839 | 0.893 | 0.629 | 20 | 1.024e+09 | 1280.0 |

DISLOCATIONS

Fig. S1 shows the total dislocation length per cascade as a function of PKA energy. The lengths are further divided into vacancy and interstitial-type dislocations, and the two Burgers vectors. The dislocations are identified with the DXA algorithm [?].

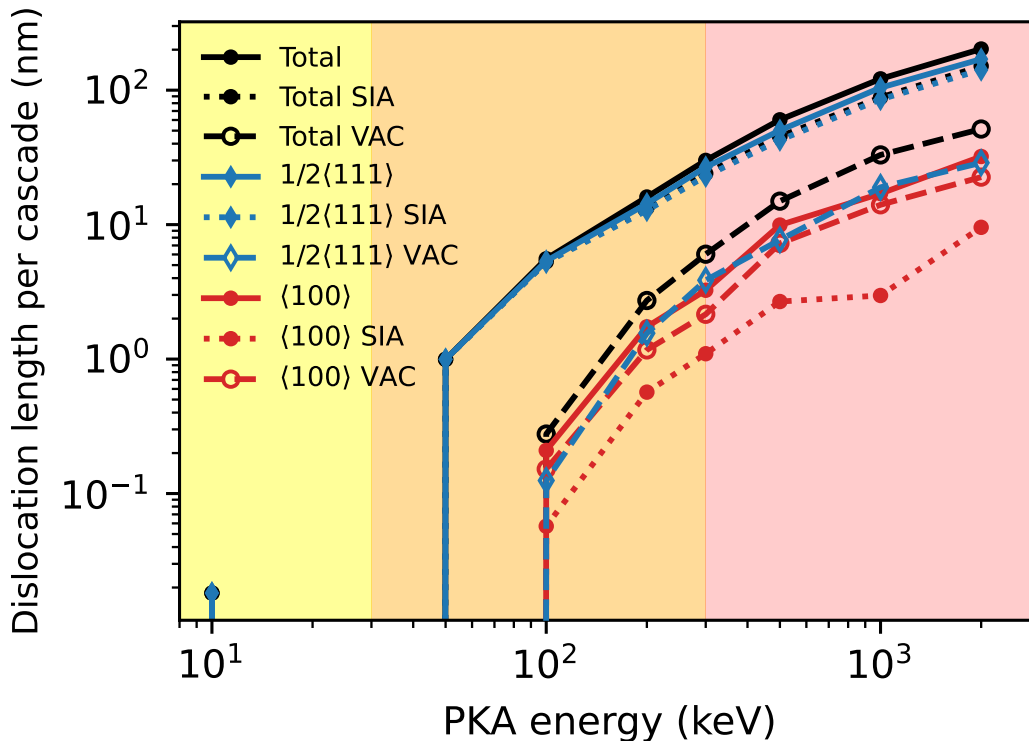


FIG. S1: Average total dislocation lengths produced in cascades as function of PKA energy. The background colors divide the energy range into the different regimes described in the main text (the lowest regime produces no dislocations and is not visible here).

CLUSTER DISTRIBUTIONS

Fig. S2 shows the cluster size distributions for vacancy and interstitial clusters for all simulated PKA energies above and including 2 keV.

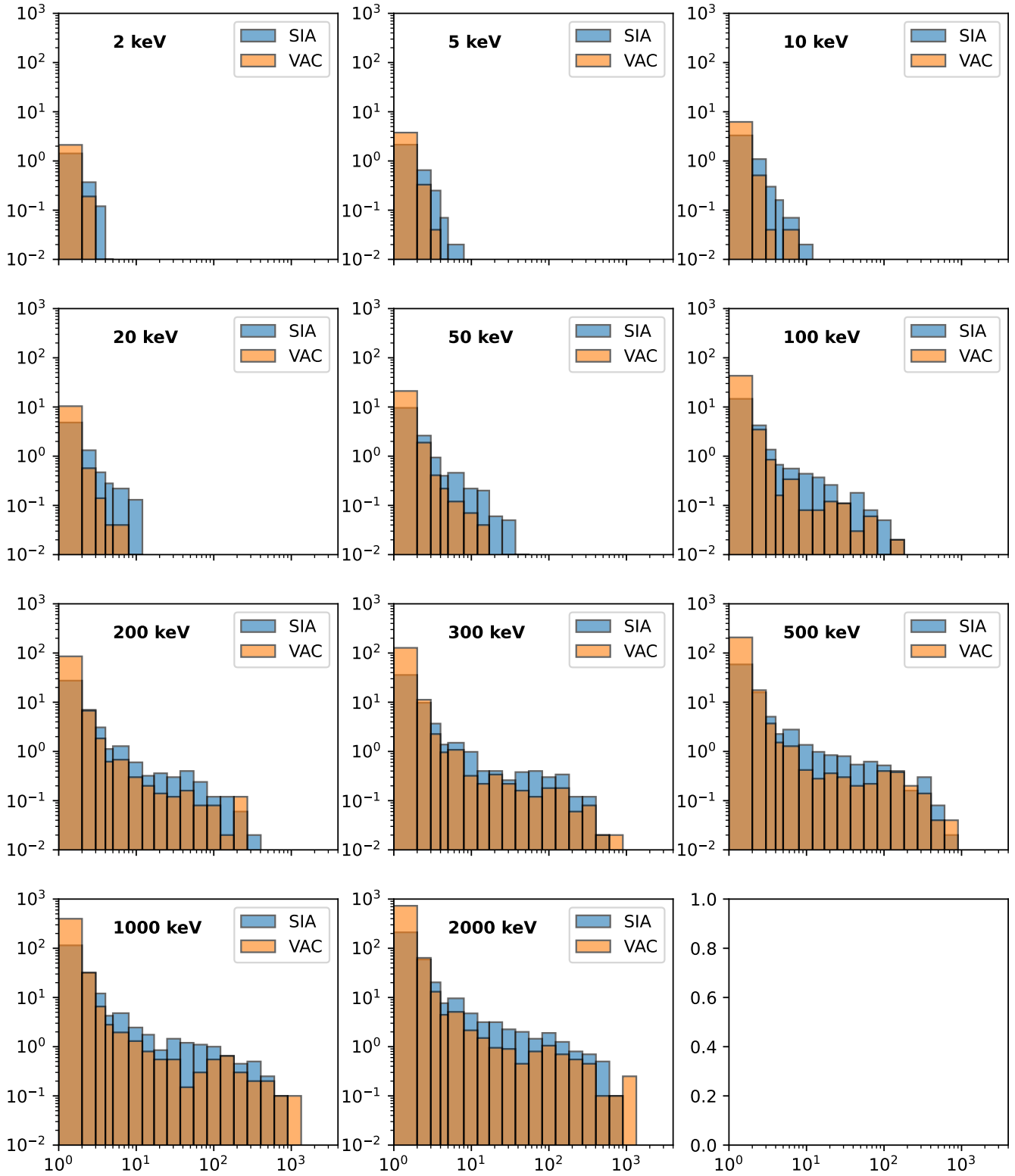


FIG. S2: Cluster size distributions for all PKA energies 2 keV and above for both vacancy and self-interstitial atom clusters.